

# Atom-interferometry constraints on dark energy

Paul Hamilton, Matt Jaffe, Philipp Haslinger, Quinn Simmons, and Holger Müller\*  
*Department of Physics, 366 Le Conte Hall MS 7300,  
 University of California, Berkeley, California 94720, USA*

Justin Khoury  
*Center for Particle Cosmology, Department of Physics and Astronomy,  
 University of Pennsylvania, Philadelphia, PA 19104, USA*

If dark energy — which drives the accelerated expansion of the universe — consists of a new light scalar field, it might be detectable as a “fifth force” between normal-matter objects, in potential conflict with precision tests of gravity. There has, however, been much theoretical progress in developing theories with screening mechanisms, which can evade detection by suppressing forces in regions of high density, such as the laboratory. One prominent example is the chameleon field. We reduce the effect of this screening mechanism by probing the chameleon with individual atoms rather than bulk matter. Using a cesium matter-wave interferometer near a spherical mass in an ultra-high vacuum chamber, we constrain a wide class of dynamical dark energy theories. Our experiment excludes a range of chameleon theories that reproduce the observed cosmic acceleration.

PACS numbers:

Cosmological observations have now firmly established that the universe is expanding at an accelerating pace, which can be explained by dark energy permeating all of space and accounting for  $\sim 70\%$  of the energy density of the universe [1]. What constitutes dark energy, and why it has its particular density, remain as some of the most pressing open questions in physics. What is clear is that dark energy presents us with a new energy scale, of order meV. It is natural to speculate that new (usually scalar) fields might be associated with that scale that make up all or part of the dark energy density [2, 3]. String theory with compactified extra dimensions, for instance, features a plethora of scalar fields, which typically couple directly to matter fields (unless protected by a shift symmetry as for axions [4, 5]). If the fields are light, this coupling would be observable as a “fifth force”, in potential conflict with precision tests of gravity [6].

In recent years, there has been much theoretical progress in developing scalar field theories that couple to matter but nonetheless evade experimental constraints — see [7] for a recent review. These theories rely on so-called screening mechanisms, which suppress the effects of the field in regions of high matter density. One prominent example is the chameleon field, whose mass depends on the ambient matter density [8–12]. It is light and mediates a long-range force in sparse environments, such as the cosmos, but becomes massive and thus short-ranged in a high-density environment, such as the laboratory. This makes it difficult to detect by fifth-force experiments.

It has recently been proposed to use atom interferometers to search for chameleons. An ultrahigh-vacuum

chamber containing atomic test particles simulates the low-density conditions of empty space, liberating the chameleon field to become long-ranged and, thus, measurable [13]. Here, we use a cavity-based atom interferometer [14–16] measuring the force between cesium-133 atoms and an aluminum sphere to search for a range of screened dark energy theories that can reproduce the current dark energy density but were out of the reach of previous experiments (Fig. 1 A). Though we focus on chameleons for concreteness, more broadly our results constrain other scalar field theories, such as symmetron [18, 19], varying-dilaton [20, 21], and  $f(R)$  theories [22, 23]. Dark energy aside, ruling out chameleons restricts a so-far untested deviation from Einstein’s equivalence principle and confirms our current understanding of space and time.

The chameleon dark energy field  $\phi$  in equilibrium is determined by minimizing a potential density  $V(\phi) + V_{\text{int}}$ , which is the sum of a self-interaction term  $V(\phi)$  and a term  $V_{\text{int}}$  describing the chameleon’s interaction with ordinary matter. The simplest chameleon theories are characterized by two parameters having the dimension of mass. The first one,  $\Lambda$ , enters the self-interaction potential [24], which we take to be of the so-called “tracker” form [25] (in natural units)

$$V(\phi) = \Lambda^4 e^{\Lambda^n/\phi^n} \simeq \Lambda^4 + \frac{\Lambda^{4+n}}{\phi^n} + \dots \quad (1)$$

The term proportional to  $1/\phi^n$  leads to screening while the constant term is responsible for the chameleon’s energy density in otherwise empty space. It can drive cosmic acceleration today if  $\Lambda = \Lambda_0 \sim 2.4$  meV, given by the current density of dark energy of  $7 \times 10^{-27}$  kg/m<sup>3</sup>; roughly the mass of four hydrogen atoms per cubic meter. The second parameter,  $M$ , enters the interaction with ordinary matter of density  $\rho$  (again using natural

---

\*Lawrence Berkeley National Laboratory, One Cyclotron Road, Berkeley, California 94720, USA; Electronic address: hm@berkeley.edu

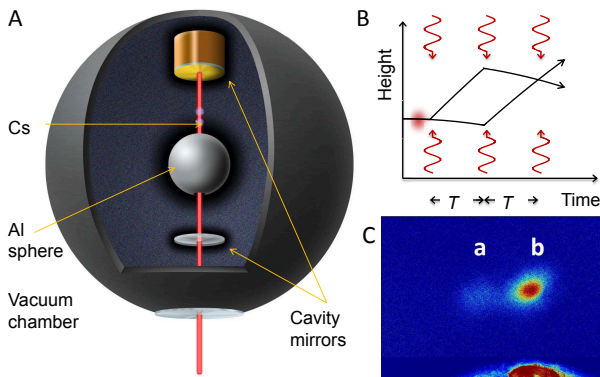


FIG. 1: (A): The vacuum chamber holds a pair of mirrors forming a Fabry-Pérot cavity and the aluminum (Al) source sphere. Laser beams pass a 1.5-mm radius hole in the  $r_s = 9.5$ -mm radius sphere. The chameleon field is suppressed close to the sphere, generating a field gradient. We form a Mach-Zehnder interferometer using cesium atoms from a magneto-optical trap (not shown). (B): Photons in three flashes of laser radiation resonant in the cavity impart momentum to the atoms, directing each atomic matter wave on two paths. The chameleon field gradient causes a phase shift between the partial matter waves. This changes the probabilities of the atoms to emerge at the two outputs of the interferometer. (C) Photograph showing the fluorescence of atoms in the two output ports (a, b) of the atom interferometer after they have been separated horizontally for detection [17]. The upper section of the picture is background-subtracted and its contrast scaled to show the sphere and atoms in one image.

units)

$$V_{\text{int}} = \frac{\phi}{M} \rho. \quad (2)$$

The parameter  $M$  is essentially unconstrained, but should plausibly be below the Planck mass  $M_{\text{Pl}} \sim 10^{19}$  GeV. A lower bound  $M > 10^4$  GeV was derived from hydrogen spectroscopy [26]. There is thus a vast range of mostly unconstrained parameter space [13].

The best existing experimental bounds [13, 27] for  $M < M_{\text{Pl}}$  come from oscillations of rubidium atoms in a harmonic trap [28] and neutrons bouncing on a surface [29]. These experiments do not rule out a chameleon at the  $\Lambda_0$  scale, where it would reproduce the current density of dark energy [13]. Limits from astrophysical observations [7] and torsion balance experiments [6, 30] are available but currently only for  $M \approx M_{\text{Pl}}$  or  $M \gtrsim M_{\text{Pl}}$ , respectively, where the chameleon force is unscreened. Other experiments such as the CHameleon Afterglow SEarch, CHASE [31] and the Axion Dark Matter eXperiment, ADMX [32], place bounds if one assumes an additional coupling of the chameleon to the photon. Our experiment does not depend on this additional coupling.

Figure 1 A shows the principle of our chameleon search. An aluminum sphere inside the ultrahigh vacuum chamber suppresses the chameleon field through the screening mechanism near its surface. An atom interferometer

(Fig. 1 B, C) with cesium atoms probes the potential difference between the interferometer arms. The field gradient accelerates the atoms and thus causes a phase shift between the interferometer arms that is measurable by counting the atoms emerging at the two outputs. The result can be compared with the theoretical prediction to yield limits on the range of viable theories.

The acceleration of an atom at a radius  $r$  from the center of the sphere caused by the chameleon interaction and gravity is given by [13]

$$a \approx \frac{Gm_s}{r^2} \left[ 1 + 2\lambda_a \lambda_s \left( \frac{M_{\text{Pl}}}{M} \right)^2 \right], \quad (3)$$

where  $G$  is the gravitational constant and  $m_s$  the mass of the sphere. The screening factors  $\lambda_a$  and  $\lambda_s$  for the atom and the sphere, respectively, approach 1 for small and light particles [17]. For macroscopic objects, however, they are much smaller than one, suppressing the chameleon force. Macroscopic fifth-force experiments are faced with two small screening factors but atom interferometers avoid this double suppression. The atoms are close realizations of the textbook concept of a light test particle. Moreover, their interaction with the environment is well understood and reproducible, which allows us to place the source object close to the atomic sample while controlling unwanted interactions from, e.g., electric and magnetic fields.

The operation of the atom interferometer is based on the matter-wave concept of quantum mechanics. When the atom absorbs or emits a photon, it recoils with the momentum  $\hbar k$  (where  $\hbar$  is the reduced Planck constant and  $k$  the wavenumber of the photon). We use a two-photon Raman transition between the two hyperfine levels of the ground state of cesium, which are labeled by their total angular momentum quantum numbers of  $F = 3$  and 4, respectively. The transition is driven by two vertical, counterpropagating laser beams, see Fig. 1 A. The atom absorbs a photon from the first beam and is stimulated by the second beam to emit a photon into the opposite direction. The net effect on the atom is a change of the internal quantum state from  $F = 3$  to  $F = 4$  and an impulse of  $\hbar k_{\text{eff}}$ , where the effective wavenumber  $k_{\text{eff}}$  is the sum of the wavenumbers of the two beams. The duration and intensity of the laser pulses can be tuned such that the transfer happens with 50% probability or nearly 100%, forming beam splitters and mirrors, respectively, for matter waves.

Our Mach-Zehnder interferometer (Figure 1 B) uses a sequence of three light pulses separated by equal time intervals  $T$ . The first pulse splits the matter-wave packet describing each atom into two partial ones that separate with a recoil velocity of about 7 mm/s. The second acts as a mirror that reverses the direction of the relative motion, and the third is a beam splitter that overlaps the partial wave packets. Interference of the partial matter waves determines the probability  $P$  of the atoms to arrive

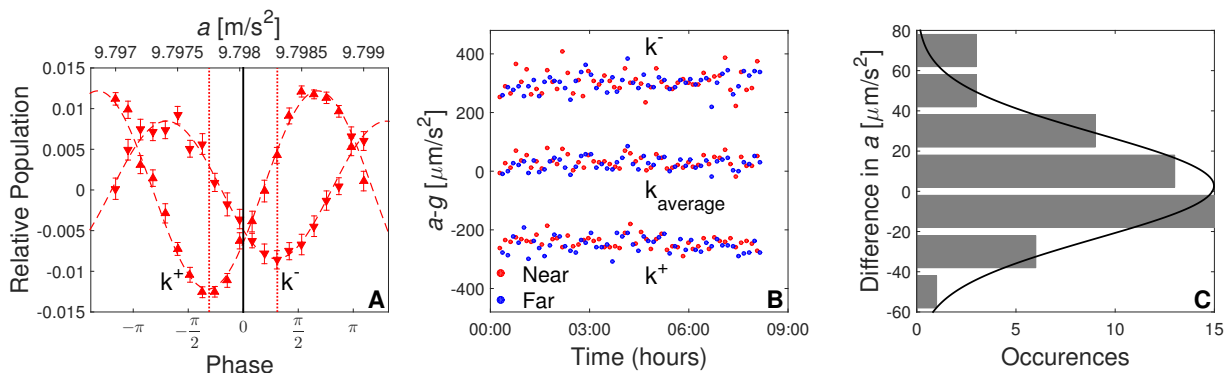


FIG. 2: (A): Two interference fringes for wavevectors  $k^\pm$  of both directions. (B) Acceleration  $a - g$ , where  $g = 9.798 \text{ m/s}^2$ , measured with wavevector-reversal and sphere near (red) and far (blue). The top group of data has the wavevector pointing downward, the bottom group upward. The plotted data is from a total of 16,800 runs. Taking the average (middle) suppresses systematic effects. Data taken during the night before about 6:30 shows lowest noise, suggesting that our sensitivity is limited by vibrations. (C) Histogram of differences between subsequent measurements with the sphere in the near and far positions.

in each of the two interferometer outputs,

$$P = \cos^2(\Delta\phi/2), \quad (4)$$

where the phase difference accumulated between the partial wave packets

$$\Delta\phi = k_{\text{eff}} a T^2 \quad (5)$$

is a function of the acceleration  $a$  of the atoms, and therefore sensitive to the chameleon.

The most sensitive atom interferometers use pulse separation times  $T$  on the order of 1 s, over which the atoms fall up to  $\sim 10 \text{ m}$  in tall atomic fountains [33–35]. We, however, must keep the atoms within the region of highest chameleon field gradient, a few millimeters, and are thus constrained to  $T$  on the order of 10 ms, resulting in only  $\sim 10^{-4}$  times the phase of large setups. Our cavity-based atom interferometer [16, 36] reaches relatively high resolution and reproducibility under these constraints.

A single operation of the atom interferometer takes 1.7 seconds. We prepare about 10 million cesium atoms at a temperature of 5 microkelvin in the  $F = 3$  state, using a two-dimensional magneto-optical trap (2D-MOT) to load a 3D-MOT through a differential pumping stage. This keeps the background pressure in the main vacuum chamber at  $\sim 6 \times 10^{-10}$  Torr. We run the interferometer with a pulse separation time of  $T = 15.5 \text{ ms}$  and detect the two outputs separately using fluorescence detection with a CCD camera [17]. Figure 1 C shows the two populations.

Figure 2 A shows an interference fringe obtained by measuring the atom number at the two interferometer outputs while varying the phase  $\Delta\phi$  [16, 17]. Fitting the fringe with a sinusoid determines the total acceleration  $a$  of the atoms.

To take out systematic effects, we apply wavevector-reversal, i.e., we change the direction of the photon impulse by reversing the two counterpropagating laser beams. This inverts the signal due to accelerations.

Many systematic effects, however, do not depend on the beam direction but only the beam intensity and can thus be taken out [37, 38]. In order to separate the chameleon force from Earth’s gravity, we compare the acceleration with the sphere located in “near” and “far” positions relative to the atoms, where near means an effective distance (averaged over the time of flight of the interferometer) of 8.8 mm (measured from the surface of the sphere) below the atoms and far means about 3 cm to the side. The sphere is moved by a computer-controlled translation stage that toggles the sphere’s position about ten times per hour.

One measurement consists of four interference fringes, one each with the wavevector normal and inverted, with the sphere near and far. Figure 2 B shows 50 such measurements with their statistical error bars. For each, we determine the average measured with normal and inverted wavevector, and compare the acceleration measured with the sphere nearby and far. Figure 2 C shows a histogram of the acceleration differences. Fitting a Gaussian to the histogram results in an estimate of  $a = (2.7 \pm 3.3) \mu\text{m/s}^2$ . We add corrections for systematic effects (ac Stark effect, magnetic fields, and electrostatic fields [17]) and arrive at  $a = (-0.7 \pm 3.7) \mu\text{m/s}^2$ , where positive  $a$  indicates acceleration towards the sphere. The two-sigma (95%) confidence interval for this data is  $-8.2 \mu\text{m/s}^2 < a < +6.8 \mu\text{m/s}^2$ .

A chameleon has spin 0 and can therefore only produce attractive forces (assuming universal coupling to matter). For this situation, we may use a one-tailed test and obtain  $a < 5.5 \mu\text{m/s}^2$  at 95% confidence level. Figure 3 shows the excluded range of parameters  $\Lambda$  and  $M$  for different exponents  $n$  alongside previous limits. The excluded range is below  $\Lambda_0 = 2.4 \text{ meV}$  for a range of  $M$  (for example,  $M < 6.6 \times 10^{-4} M_{\text{Pl}}$  for  $n = 1$ ), thus ruling out chameleons that reproduce the acceleration of the cosmos. The figure also shows the two best limits from previous experiments [13, 28, 29]. While our analysis

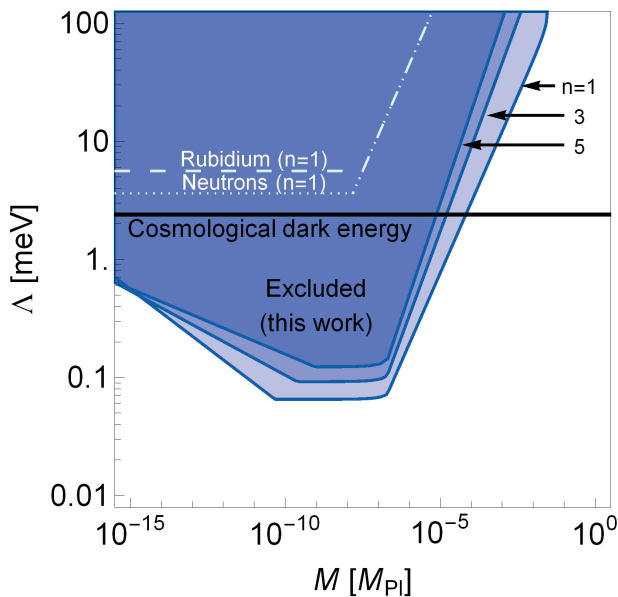


FIG. 3: Region of exclusion at 95% confidence level. Three limits are shown for exponents  $n = 1, 3,$  and  $5$  in the self-interaction potential Eq. (1), respectively. Dashed lines are previous limits [28, 29], available for  $n = 1$ . (For previous limits outside the plotted area, see the introduction.) The gray horizontal line and its width mark the range around  $\Lambda_0 = 2.4 \text{ meV}$  where the chameleon field would reproduce the current cosmic acceleration.

was specific to chameleons, the experiment is applicable to other types of screened scalar-field models for dark energy.

Future atom interferometers can further increase the coverage of Fig. 3, e.g., at high  $M$ . Interferometry with lighter atoms such as lithium could improve the sensitivity in the regions where even the atom is screened. Experiments with ultra-low-density sources such as aerogel could broaden the search for chameleons having low quantum corrections [17].

We acknowledge important discussions with Dimitry Budker, Clare Burrage, Yasunori Nomura, Saul Perlmutter, Surjeet Rajendran, and Paul Steinhardt. This work was supported by the David and Lucile Packard Foundation, the Defense Advanced Research Projects Agency, the National Science Foundation, and the National Aeronautics and Space Administration. P. Haslinger thanks the Austrian Science Fund (FWF): J3680. The work of JK is supported by NSF CAREER Award PHY-1145525 and NASA ATP grant NNX11AI95G. This paper is dedicated to Martin Perl with gratitude.

- 
- [1] [Planck Collaboration], arXiv:1502.01589 [astro-ph.CO].
  - [2] C. Wetterich, Nucl. Phys. B **302**, 668 (1988).
  - [3] P. J. E. Peebles and B. Ratra, Astrophys. J. **325**, L17 (1988).
  - [4] J. A. Frieman, C. T. Hill, A. Stebbins and I. Waga, Phys. Rev. Lett. **75**, 2077 (1995).
  - [5] K. Choi, L. J. Hall, Y. Nomura and S. J. Oliver, Phys. Rev. Lett. **95**, 141302 (2005).
  - [6] D. J. Kapner *et al.*, Phys. Rev. Lett. **98**, 021101 (2007).
  - [7] A. Joyce, B. Jain, J. Khoury and M. Trodden, arXiv:1407.0059 [astro-ph.CO], Phys. Rep., in press.
  - [8] J. Khoury and A. Weltman, Phys. Rev. D **69**, 044026 (2004).
  - [9] J. Khoury and A. Weltman, Phys. Rev. Lett. **93**, 171104 (2004).
  - [10] S. S. Gubser and J. Khoury, Phys. Rev. D **70**, 104001 (2004).
  - [11] D. F. Mota and D. J. Shaw, Phys. Rev. Lett. **97**, 151102 (2006).
  - [12] D. F. Mota and D. J. Shaw, Phys. Rev. D **75**, 063501 (2007).
  - [13] C. Burrage, E. J. Copeland and E. A. Hinds, arXiv:1408.1409 [astro-ph.CO].
  - [14] M. Kasevich and S. Chu, Phys. Rev. Lett. **67**, 181 (1991).
  - [15] A. D. Cronin, J. Schmiedmayer, and D. E. Pritchard, Rev. Mod. Phys. **81**, 1051 (2009).
  - [16] P. Hamilton *et al.*, arXiv:1409.7130 [physics.atom-ph], Phys. Rev. Lett., in press.
  - [17] See the supplementary materials.
  - [18] K. Hinterbichler and J. Khoury, Phys. Rev. Lett. **104**, 231301 (2010).
  - [19] K. A. Olive and M. Pospelov, Phys. Rev. D **77**, 043524 (2008).
  - [20] T. Damour and A. M. Polyakov, Nucl. Phys. B **423**, 532 (1994);
  - [21] P. Brax, C. van de Bruck, A. C. Davis, B. Li and D. J. Shaw, Phys. Rev. D **83**, 104026 (2011).
  - [22] S. Capozziello, S. Carloni and A. Troisi, Recent Res. Dev. Astron. Astrophys. **1**, 625 (2003).
  - [23] S. M. Carroll, V. Duvvuri, M. Trodden, and M. S. Turner, Phys. Rev. D **70**, 043528 (2004).
  - [24] P. Brax, C. van de Bruck, A. C. Davis, J. Khoury, and A. Weltman, Phys. Rev. D **70**, 123518 (2004).
  - [25] I. Zlatev, L. M. Wang, and P. J. Steinhardt, Phys. Rev. Lett. **82**, 896 (1999).
  - [26] P. Brax and C. Burrage, Phys. Rev. D **83**, 035020 (2011).
  - [27] P. Brax, C. van de Bruck, A. C. Davis, D. F. Mota, and D. J. Shaw, Phys. Rev. D **76**, 124034 (2007).
  - [28] D. M. Harber, J. M. Obrecht, J. M. McGuirk, and E. A. Cornell, Phys. Rev. A **72**, 033610 (2005).
  - [29] T. Jenke *et al.*, Phys. Rev. Lett. **112**, 151105 (2014).
  - [30] A. Upadhye, Phys. Rev. D **86**, 102003 (2012).
  - [31] J. H. Steffen *et al.* [GammeV Collaboration], Phys. Rev. Lett. **105**, 261803 (2010).
  - [32] G. Rybka *et al.* [ADMX Collaboration], Phys. Rev. Lett. **105**, 051801 (2010).
  - [33] S.-Y. Lan *et al.*, Science **339**, 554 (2013).
  - [34] G. Rosi, F. Sorrentino, L. Cacciapuoti, M. Prevedelli,

- and G.M. Tino, *Nature* **510**, 518 (2014).
- [35] A. Sugarbaker, S. M. Dickerson, J. M. Hogan, D. M. S. Johnson, M. A. Kasevich, *Phys. Rev. Lett.* **111**, 113002 (2013).
- [36] M. A. Hohensee, B. Estey, P. Hamilton, A. Zeilinger and H. Müller, *Phys. Rev. Lett.* **108**, 230404 (2012).
- [37] J. M. McGuirk, G. T. Foster, J. B. Fixler, M. J. Snadden and M. A. Kasevich, *Phys. Rev. A* **65**, 033608 (2002).
- [38] D. Schlippert *et al.* *Phys. Rev. Lett.* **112**, 203002 (2014).
- [39] D.S. Weiss, B.C. Young, and S. Chu, *Appl. Phys. B.* **59**, 217-256 (1994).

## Appendix A: Chameleon force equations

We treat Eq. (3) as resulting from a quantum effective potential, as is common [13]. We assume a universal coupling to matter for simplicity, though our analysis can straightforwardly be generalized to chameleons that couple with different strength to different matter species. To predict the force, we follow [13] but generalize to the case of  $n \neq 1$  in Eq. (1). We assume a sphere of radius  $r_s$ , density  $\rho_s$ , and mass  $m_s$ , and model the atoms as spheres having the nuclear mass  $m_a$ , radius  $r_a$ , and density  $\rho_a$ . This is a conservative choice, as using the larger radius and smaller average density of the entire atom would lead to sharper bounds. Our choice of a  $r = 9.5$  mm sphere is to optimize the sensitivity throughout the  $\Lambda - M$  plane shown in Fig 3. The acceleration of the atom resulting from the chameleon is given by Eq. (3). When an object is screened, the chameleon is long-ranged only in a thin shell of radius,  $s_i$ , near the surface of the object. The screening factors are [13] (this section uses natural units  $c = \hbar = 1$  throughout)

$$\lambda_i \simeq \begin{cases} 1; & \rho_i r_i^2 < 2M\phi_{bg} \\ 1 - \frac{s_i^3}{r_i^3}; & \rho_i r_i^2 > 2M\phi_{bg} \end{cases}, \quad (\text{A1})$$

where the index  $i = a, s$  denotes the atom and the sphere, respectively. The radius of the thin shell is given by  $s_i = r_i \sqrt{1 - 2M\phi_{bg}/(\rho_i r_i^2)}$ , where  $\phi_{bg}$  is the background field value inside the vacuum chamber. If  $\lambda_i < 1$ , the field is suppressed everywhere inside the object except within a thin shell near the surface, and hence the force is suppressed.

The background field value,  $\phi_{bg}$ , is the smallest of  $\phi_{eq}$ , the equilibrium value for the residual gas inside the vacuum chamber, and  $\phi_{vac}$ , which is set by the size of the chamber:

$$\phi_{bg} = \min(\phi_{eq}, \phi_{vac}). \quad (\text{A2})$$

For a generalized potential Eq. (1),  $\phi_{eq}$  is determined by the equilibrium condition

$$-\frac{n\Lambda^{4+n}}{\phi_{eq}^{n+1}} + \frac{\rho_v}{M} = 0, \quad (\text{A3})$$

where  $\rho_v$  is the average density of residual gas in the chamber, which is mostly hydrogen. Therefore,

$$\phi_{eq} = \left( \frac{nM\Lambda^{4+n}}{\rho_v} \right)^{\frac{1}{1+n}}. \quad (\text{A4})$$

Meanwhile, the vacuum value  $\phi_{vac}$  is such that the chameleon Compton wavelength is comparable to the characteristic size  $r_v$  of the vacuum chamber:

$$m_{vac}^2 = \left. \frac{\partial^2 V}{\partial \phi^2} \right|_{vac} = \frac{n(n+1)\Lambda^{4+n}}{\phi_{vac}^{n+2}} \propto \frac{1}{r_v^2}. \quad (\text{A5})$$

In other words,

$$\phi_{vac} = \xi (n(n+1)\Lambda^{4+n} r_v^2)^{\frac{1}{n+2}}. \quad (\text{A6})$$

The order-unity factor  $\xi$  depends on the geometry of the vacuum chamber and can be obtained by numerically solving the chameleon equation of motion. To do so, we model the vacuum chamber as two simple geometries: *i*) a sphere; *ii*) an infinite cylinder. In both cases, the chameleon equation reduces to an ordinary differential equation, which can be integrated straightforwardly. For this purpose, we neglect the chamber walls, and impose that  $\phi \rightarrow \phi_{\text{atm}}$  (the equilibrium value for atmospheric density) far from the chamber.

It turns out that  $\xi$  is largely insensitive to  $M$ ,  $\Lambda$  and  $r_v$ . For example, for  $n = 1$  we find

$$\xi \simeq \begin{cases} 1.8 & \text{(sphere)} \\ 1.6 & \text{(cylinder)} \end{cases}. \quad (\text{A7})$$

These two values yield nearly indistinguishable exclusion regions in Fig. 3. Since the actual chamber is neither a sphere nor an infinite cylinder, we adopt the smaller value of  $\xi$  as a conservative approximation to the actual geometry.

These equations predict the acceleration  $a$  of atoms in our vacuum chamber. For experimental convenience, we will express it in units of the earth's acceleration of free fall,  $g = \frac{4}{3}G\pi r_{\oplus}\rho_{\oplus}$ , where  $r_{\oplus}$  and  $\rho_{\oplus}$  respectively denote earth's radius and density.

Figure 3 shows our bounds for theories with the exponent  $n = 1, 3, 5$ . Following one of them from the left (low  $M$ ) to the right, we may distinguish three regions in which the exclusion boundary first points downward (i), then horizontally (ii), and finally upwards (iii). A fourth region (iv) lies to the right of the figure and would have the contour pointing vertically upwards.

In region (i), both the source and the test mass are screened and the chameleon field reaches its equilibrium value in the vacuum chamber. In this region, the acceleration can be expressed as

$$\frac{a}{g} \approx \frac{18M_{\text{Pl}}^2}{r_s\rho_a r_a^2\rho_{\oplus}r_{\oplus}} \left( \frac{nM\Lambda^{4+n}}{\rho_v} \right)^{\frac{2}{n+1}} \frac{r_s^2}{r^2}. \quad (\text{A8})$$

Close to the sphere surface, where  $r_s^2/r^2 \sim 1$ , this acceleration is large for a small source radius, atom mass, and low vacuum pressure. In the next regime (ii), both the test and source masses are shielded. The chameleon force

$$\frac{a}{g} \approx \frac{18M_{\text{Pl}}^2}{r_s\rho_a r_a^2\rho_{\oplus}r_{\oplus}} \xi^2 (n(n+1)\Lambda^{4+n}r_v^2)^{\frac{2}{n+2}} \frac{r_s^2}{r^2} \quad (\text{A9})$$

is large for a large vacuum chamber and small source radius and atom mass. Going to region (iii) in the direction of higher  $M$ , the atoms become unscreened but the source mass is still screened. Here the acceleration

$$\frac{a}{g} \approx \frac{6M_{\text{Pl}}^2}{Mr_s\rho_{\oplus}r_{\oplus}} \xi (n(n+1)\Lambda^{4+n}r_v^2)^{\frac{1}{n+2}} \frac{r_s^2}{r^2} \quad (\text{A10})$$

can be increased by a large vacuum chamber radius and small source radius but is independent of the atom mass.

Finally, in region (iv), neither the sphere nor the atoms are screened and the acceleration of the test particle is

$$\frac{a}{g} \approx \frac{2M_{\text{Pl}}^2}{M^2} \frac{\rho_s r_s^3}{r^2 r_{\oplus} \rho_{\oplus}}, \quad (\text{A11})$$

independent of  $\Lambda$ . In this region, the sensitivity can be increased linearly by increasing the density or the radius of the source object.

## Appendix B: Setup

The chameleon force's counter-intuitive behavior informs the design of our setup. A small atomic mass is helpful in regions (i, ii), but the relatively large mass of cesium helps restricting the spatial extent of the atom interferometer by lowering the recoil velocity. This helps us to operate close to the source sphere. A small source radius helps in regions (i-iii), with 1 cm being a good compromise with mechanical requirements.

Our setup has been described in [16]; we only give the essential details here. We cool the atoms in a magneto-optical trap (MOT) followed by sub-Doppler cooling and optical pumping into the magnetically insensitive  $F = 4, m_F = 0$  quantum state. This leads to  $\sim 2 \times 10^8$  cesium atoms at a temperature of about  $5 \mu\text{K}$ . We purify the  $m_F = 0$  state by two state-sensitive Raman transitions and select a velocity subgroup by a  $12\mu\text{s}$ , velocity-sensitive Raman pulse.

The cavity consists of a piezo-driven, flat gold mirror and one dielectric mirror having 5 m radius of curvature. The fundamental longitudinal mode of the cavity has a beam waist of  $600 \mu\text{m}$  (located at the surface of the flat mirror), a finesse of  $\mathcal{F} = 100$ , and a linewidth of 3.6 MHz. The transverse modes of the cavity are non-degenerate in resonance frequency. The length of the cavity (40.756 cm) allows two frequencies separated by the cesium hyperfine splitting of  $\sim 9.2 \text{ GHz}$  to be simultaneously near-resonant.

The frequency pair is generated from a single laser with low phase noise by a fiber-coupled broadband electro-optic modulator (Eospace). All lasers are diode lasers and frequency stabilized (locked) to a reference laser, which is in turn stabilized to a cesium transition by modulation transfer spectroscopy. The cavity length is stabilized to a tracer laser whose wavelength of 780 nm is far from any transition in cesium and has a negligible effect on the atoms.

We ramp the difference frequency in the Raman frequency pair at a rate of  $r \sim 2\pi \times 23 \text{ MHz/s}$  so that the beams remain resonant as the freely falling atoms accelerate.

Our normalized detection works by pushing atoms in  $F = 4$  to the side with our clearing beams, leaving atoms in  $F = 3$  behind, and then using fluorescence detection of both populations with a CCD camera, see Fig. 1 C.

TABLE I: Corrections for systematic errors and their 1-sigma uncertainties.

Quantity	Correction	Uncertainty
	$\mu\text{m/s}^2$	$\mu\text{m/s}^2$
Magnetic fields	-4.5	1.7
Ac Stark effect	1.1	0.50
Surface voltage	-	0.08
Total	-3.4	2.1

### Appendix C: Systematic effects

Systematic effects that are independent of the sphere position are cancelled out in our experiment. This suppresses many systematics typical in atom interferometers to negligible levels, e.g., the Gouy phase and wavefront curvature, laser frequency variations, gravity and gravity gradients, atom density- and index of refraction effects. Table I gives an overview of the remaining systematic corrections and errors.

#### 1. Magnetic fields

A change in magnetic field can lead to a systematic shift due to the quadratic Zeeman shift of  $0.43 \text{ kHz/G}^2$  of the hyperfine splitting of cesium in the  $m_F = 0$  ground state. The symmetry of the Mach-Zehnder interferometer makes a shift from a constant magnetic field common to both interferometer arms. However, a magnetic field gradient  $B'$  on top of a constant bias field  $B_0$  can add an effective force on the atoms that is proportional to  $B_0 B'$  and thus linear in the bias field. This force may be different for measurements with the sphere in the near and far locations due to small changes the MOT position induced, e.g., by slight partial blocking of the MOT beams. To characterize the shift, we run the interferometer at bias fields  $B_0$  up to ten times the value of  $133 \text{ mG}$  used for data taking. Figure 4 shows the change in measured differential acceleration relative to the reference point at  $133 \text{ mG}$ . Extrapolating to zero field, we find a systematic shift of  $(-4.5 \pm 1.7) \mu\text{m/s}^2$ .

#### 2. Ac Stark effect

The ac Stark effect is an energy-level shift of the atoms induced by the Raman laser pulses [39]. While wavevector reversal eliminates this effect to leading order, for large changes in the ac Stark shift between pulses, a small second-order influence may remain.

To characterize this remaining influence, we increase it by varying the laser intensity by  $\pm 20\%$ , much more than the routine intensity changes during our measurement. Figure 5 shows the changes in the acceleration measurement along with their one-sigma confidence interval. Near the nominal laser power  $P_0$  without sphere,

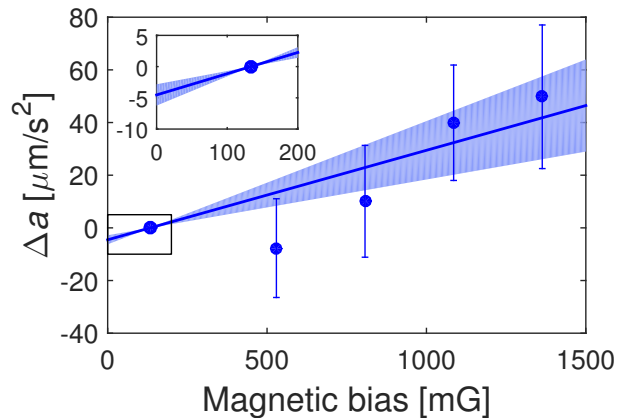


FIG. 4: Measurement of the differential acceleration between sphere in the near and far positions versus magnetic bias field. The shaded area is the one-sigma confidence interval (non-simultaneous function prediction interval) determined from statistics over 1176 experimental runs (7 fringes per point per wavevector direction and sphere position). The inset shows a magnified region near 0 G.

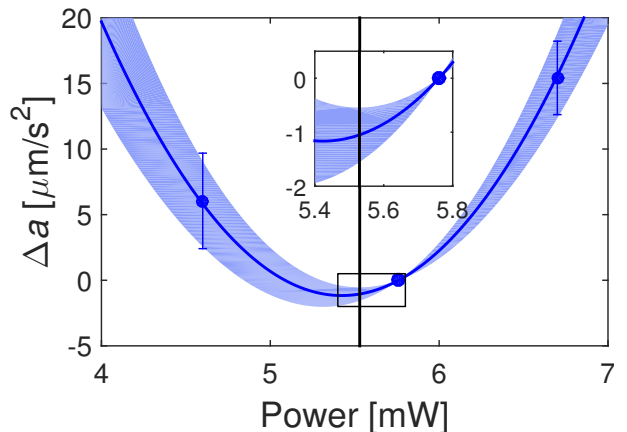


FIG. 5: Changes  $\Delta a$  in the measured acceleration relative to the acceleration measured at a nominal power of  $P_0 \sim 5.8 \text{ mW}$  with the sphere in the far position. The shaded area is the one-sigma confidence interval determined from 12096 experimental runs. The fitting model is  $\alpha(P - P_0)(P - \beta)$ , where  $\alpha$  and  $\beta$  are free parameters.

the measured acceleration is nearly independent of laser power variations. For large deviations of the power, however, a quadratic dependence is evident.

If the sphere has no effect on the interferometry laser pulses, the ac Stark shift systematic will cancel when comparing measurements with the sphere in the near and far positions. Experimentally, however, we observe that placing the sphere in the optical cavity reduces the laser intensity by  $4 \pm 1\%$ . From Fig. 5, such a reduction in sphere coupling results in a systematic correction of  $(1.1 \pm 0.5) \mu\text{m/s}^2$ .

### 3. Surface charges

While the sphere is grounded electrically, aluminum surfaces may carry surface potentials because of the approximately 4-10nm thick insulating natural passivation layer. Thin films of alumina may have a dielectric strength of up to several MV/cm, allowing for surface

voltages up to  $\sim 10$  Volts. From the ground state dc polarizability of cesium, even a surface potential of 100 V would cause an acceleration of no more than  $0.08 \mu\text{m}/\text{s}^2$  towards the sphere for atoms 5 mm from the surface. The acceleration increases quadratically with voltage. We conservatively use  $0.08 \mu\text{m}/\text{s}^2$  as an error bar on the measured acceleration.